POLITECNICO DI TORINO
Repository ISTITUZIONALE

Integrated Design and Prototyping of a 77 GHz Automotive Medium Range Radar into Car Rear Lamp

*Original*
Integrated Design and Prototyping of a 77 GHz Automotive Medium Range Radar into Car Rear Lamp / Caffa, M., Bottigliero, S., Ramonda, F., Gioanola, L., Maggiora, R.. - In: IEEE TRANSACTIONS ON VEHICULAR TECHNOLOGY. - ISSN 0018-9545. - ELETTRONICO. - 73:3(2024), pp. 3041-3050. [10.1109/TVT.2023.3324986]

*Availability:*
This version is available at: 11583/2983228 since: 2023-10-22T08:49:43Z

*Publisher:*
IEEE

*Published*
DOI:10.1109/TVT.2023.3324986

*Terms of use:*

This article is made available under terms and conditions as specified in the corresponding bibliographic description in the repository

*Publisher copyright*
IEEE postprint/Author's Accepted Manuscript

©2024 IEEE. Personal use of this material is permitted. Permission from IEEE must be obtained for all other uses, in any current or future media, including reprinting/republishing this material for advertising or promotional purposes, creating new collecting works, for resale or lists, or reuse of any copyrighted component of this work in other works.

(Article begins on next page)

27 November 2026

This article has been accepted for publication in IEEE Transactions on Vehicular Technology. This is the author's version which has not been fully edited and content may change prior to final publication. Citation information: DOI 10.1109/TVT.2023.3324986



# Integrated Design and Prototyping of a 77 GHz Automotive Medium Range Radar into Car Rear Lamp

Mattia Caffa, Stefano Bottigliero, Federico Ramonda, Luca Gioanola and Riccardo Maggiora

***Abstract*—The continuing trend of increasing the frequency adopted for automotive radar application has permitted an overall increase of performances and reduction of the dimensions of this type of device. This last feature could permit new ways of installation with respect to the standards adopted today by car manufacturer (behind bumpers or in car body). Instead of seeing the radar as an external device to be installed on the car it could be part of the initial project and included into the design process of a plug-in part.**

**In this paper the integrated design and prototyping of 77 GHz automotive radar into a modern car rear lamp is presented. The radar Printed Circuit Board (PCB) has been designed to fit into the lamp without affecting the external look; the optimization of the material thickness of the radar cover and temperature tests have been performed on the system. The embedded radar processing has been implemented on a monolithic chip to perform target tracking and the main processing steps are reported.**

**The results obtained from tests in controlled environment and on the road in traffic scenarios show that including the radar into the design of a lamp from the beginning is a feasible solution. This approach brings some advantages such as: improved placing and connections, undisturbed view, better protection from disturbances and accidents and provides more customized solutions for the car makers.**

***Index Terms*—Automotive radar, FMCW, millimiter wave radar, MIMO radar, radar integration.**

## I. Introduction

Automotive radars are key components in the development of reliable Advance Driver Assistant Systems (ADASs) [1]. An increasing number of different sensors around the vehicle such as radars, cameras and LIDARs will be required to achieve a full 360-degree view of the vehicle's surroundings. The end goal is to reach a system which satisfy Level 5 of the Society of Automotive Engineering (SAE) J3016 standard [2] classification: a fully automated vehicle in which all the systems are controlled by the ADAS and no human intervention is required. Since radars, with respect to other sensors, have better immunity to weather conditions, longer detection range, low cost, good resolution, and precise position estimation, radar technologies have been under active investigation to enable future ADAS and intelligent transportation systems [3].

Different modulation schemes for radar waveforms have been studied and adopted: the Frequency Modulated Continuous Wave (FMCW) [4] is the most popular for automotive applications due to its ease hardware requirements and low costs, but more recently digital modulation raised in popularity in the form of Orthogonal Frequency Division Multiplexing (OFDM) [5], and Phase Modulated Continuous Wave (PMCW) [6] also thanks to their ability to exploit Joint Communication and Radar Sensing (JRCS) [7], [8]. Each of these modulation have some advantages and disadvantages which have been analyzed in [9], [10] and [11].

Radars can be classified based on the detection range into Short-Range Radars (SRRs), Medium-Range Radars (MRRs) and Long-Range Radars (LRRs). Each type of radar can cover different ADAS functionalities, for example LRRs are suitable for Adaptive Cruise Control (ACC). MRRs are good for Lane Change Assist (LCA), Cross Traffic Alert (CRT) and Blind Spot Detection (BSD). SRRs are used for parking and proximity detection [12].

The increasing requests to improve angular resolution in automotive radar to separate more targets is a challenge which has been addressed using the Multiple-Input Multiple-Output (MIMO) technique [13] which creates a virtual array of receive antennas that contains more elements and has larger size than the array of physical receive antennas through the use of orthogonal transmit waveforms [14]; this technique is still heavily relied upon in automotive radar today [15] and recently different high-resolution imaging radars with cascaded radar chip and a very high number of transmitting and receiving channels (over 2000 virtual channels) have been presented [16], [17], [18]. The disadvantage of these radars is that they are power hungry and they tend to be large in size due to the area required by the antenna.

Another solution which has been investigated and still is a topic of research is the adoption of radar distributed networks [19], [20]. Distributed radar networks allow to achieve greater aperture sizes and enable finer angular resolution but they require heavy centralized processing.

Automotive radars are usually installed on cars as external black box devices to be connected to vehicle Controlled Area Network (CAN) bus. The standard placement for automotive radar sensors is in tight spots behind bumpers or emblems [21]. While this offers protection to the antenna and does not affect the visual design of the vehicle, it introduces different points of concern for the car maker. For example, long cables need to be laid in the chassis, ad hoc spots need to be created in the car body, radome and painting effects must be evaluated

Copyright (c) 2023 IEEE. Personal use of this material is permitted.Personal use of this material is permitted. However, permission to use this material for any other purposes must be obtained from the IEEE by sending a request to pubs-permissions@ieee.org.

Authorized licensed use limited to: Politecnico di Torino. Downloaded on October 22,2023 at 08:47:04 UTC from IEEE Xplore. Restrictions apply.
© 2023 IEEE. Personal use is permitted, but republication/redistribution requires IEEE permission. See https://www.ieee.org/publications/rights/index.html for more information.

This article has been accepted for publication in IEEE Transactions on Vehicular Technology. This is the author's version which has not been fully edited and content may change prior to final publication. Citation information: DOI 10.1109/TVT.2023.3324986



and mitigated.

The incorrect spacing between the bumper (usually a multi-layer structure) and the antenna can cause multiple reflections, especially when metallic paints are used. These reflections affect range and velocity estimation [22] , worsen direction of arrival estimation and degrade the Field of View (FOV) [21]. Another drawback of the bumper is the presence of mud and/or dust and ice or snow accumulating in front of the sensor which introduces disturbances that increase the noise floor and reduce detection performances as shown in the contaminated radome attenuation data reported in [23].

A part of the vehicle which has been in the discussion for the placement of radar sensors is the lamp [24]. Usually car lamps materials are thinner, adjustable, and without painting bringing consistent advantages to the above mentioned problems. Lamp housings offer higher protection from external disturbances, better protection in case of minor accidents and no need for extra-cables.

In [25], the projection lens of a lighting unit is used as an electromagnetic lens for a millimeter waves radar with waveguide antennas. In [24], an antenna integration inside a headlamp for automotive radar applications is presented. The antenna comprises the feed, which is embedded within the electronic unit, and a reflector made of transparent materials.

In this paper we propose an integrated design and prototyping of a rear lamp with a 77 GHz FMCW automotive corner MRR (75 m maximum detection range, 35° pointing angle) without affecting the external look of the lamp and its lighting functions.

The integrated design aims to combine the advantages of placing the radar into the lamp while also optimizing the radar performances by means of tuning PCB electronics, material thicknesses, position of the antennas, upgrading the software and improving thermal dissipation.

The radar installation into the lamps together with other sensors around the car would help to achieve a comprehensive 360-degree view of the vehicle's surroundings.

The structure of this paper is as follows: in Section II the FMCW radar principles are introduced; in Section III the system with the lamp and the radar is described; in Section IV the hardware design is presented; in Section V the radar parameters and some of the software implementation are given; in Section VI thermal measurements of the radar inside the lamp in heat chamber with results are shown; in Section VII the measured results captured in real-world scenarios are presented. Finally, in Section VIII conclusions are drawn.

## II. FMCW Radar Principles

A brief description of the FMCW radar principles, and signal processing are provided below. A well-described and more in-depth analysis of FMCW modulation and signals can be found in [26].

FMCW is the conventional modulation used for automotive radars, and has been adopted by manufacturers in recent decades. A certain number of frequency-modulated signals, called chirps, are transmitted periodically from an FMCW radar. The transmitted chirp can be written as,

$$s_{Tx}(t) = exp(j2\pi f_0 t + j\pi \frac{B}{T_c} t^2) \tag{1}$$

where $f_0$ is the carrier frequency, $B$ is the bandwidth and $T_c$ is the duration of each chirp. The ideal received scattered signal from a target at distance $R$ after a propagation delay $t_d = 2R/c$ where c is the speed of light is,

$$s_{Rx}(t) = A s_{Tx}(t - t_d) exp(j2\pi f_d t) \tag{2}$$

where $A$ is the amplitude, and $f_d$ is the Doppler frequency of the target.

After mixing the received signal with the transmitted signal, the low-pass filtered beat-frequency signal is obtained,

$$s_{Rxm}(t) = Aexp(-j2\pi(\frac{Bt_d}{T_c} - f_d)t) exp(j\pi \frac{Bt_d{}^2}{T_c} - j2\pi f_0 t_d) \tag{3}$$

and it is sampled with the Analog-to-Digital Converters (ADCs). The first exponential contains the target information of range and Doppler. The second exponential is a phase term which is not varying with time, it is constant across all Fast Fourier Transform (FFT) samples and it does not influence the range and Doppler calculation. The range response of the radar is derived by calculating an FFT on the beat-frequency signal. The Doppler-induced frequency variation is extracted by calculating a second FFT for each range bin along the different chirps to measure the target's velocity. By exploiting a MIMO array, angle of arrival estimation is possible due to the known positions of the antennas.

## III. System Description

The rear lamp selected for the integrated design is reported in Fig.1. The mounting angle of the lamp is 35° with respect

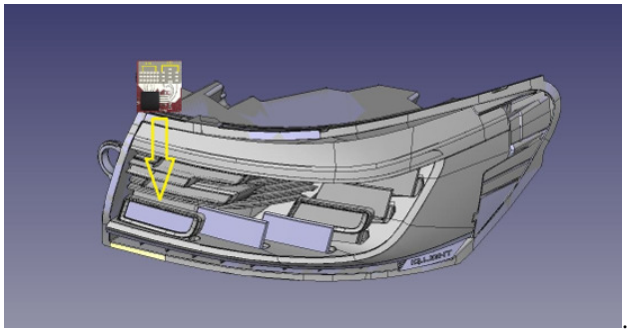


Fig. 1: Target rear lamp and radar positioned behind petal

to the car axis making it suitable for a corner radar installation. The rectangular part indicated by the arrow, hereafter referred to as the 'petal', is illuminated with Organic Light-Emitting Diode (OLED) technology from below. The petal dimensions are 60 mm X 29 mm which is an extremely small area and is a constraint for the radar board dimensions. The target application for this prototype is a medium range corner radar with a maximum vehicles detection range of 75 m. To not affect the design and the lighting, the radar board has been

Authorized licensed use limited to: Politecnico di Torino. Downloaded on October 22,2023 at 08:47:04 UTC from IEEE Xplore. Restrictions apply.
© 2023 IEEE. Personal use is permitted, but republication/redistribution requires IEEE permission. See https://www.ieee.org/publications/rights/index.html for more information.

This article has been accepted for publication in IEEE Transactions on Vehicular Technology. This is the author's version which has not been fully edited and content may change prior to final publication. Citation information: DOI 10.1109/TVT.2023.3324986



placed behind the petal. The radar board is connected to a second dedicated board for radar power supply.

A section of the lamp structure in front of the radar is shown in Fig. 2. The petal has two layers of different materials and thickness.

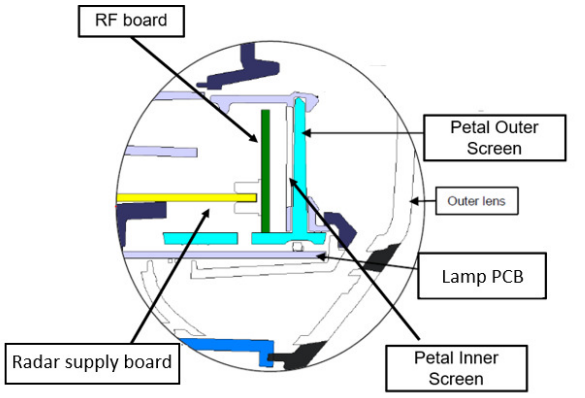



Fig. 2: Transverse cut of the lamp in front of the radar

The material transmission coefficients ($S_{21}$) of the outer lens and the petal outer and inner screen have been measured in the 60-90 GHz frequency band in order to evaluate their relative dielectric constant ($\epsilon_r$) and loss tangent (tan$\delta$).

The set up for this measurement consists of a vector network analyzer connected to a Tx and an Rx lens horn antennas and a panel of the material under test placed in between. The panel need to have an area that is large enough to reduce edge effects. The $S_{21}$ entry of the S matrix has been measured in phase and magnitude, at first with free space (air) in between the antennas and then with the panel. By comparison of the two measurements $tan\delta$ and $\epsilon_r$ have been calculated. The results of the measurements at 77 GHz are reported in Table I.

TABLE I: Lamp materials thickness and dielectic properties at 77 GHz

| Part | Thickness | $\epsilon_r$ | $tan\delta$ |
|---|---|---|---|
| Outer Lens | 3.5 mm | 1.25 | 0.007 |
| Petal Outer Screen | 2.8 mm | 3.18 | 0.03 |
| Petal Inner screen | 1.17 mm | 2.79 | 0.01 |

The multilayer structure reflection coefficient (S11) has been estimated considering normal incidence and treating the incident field on the material as plane wave. The $S_{11}$ element of the S matrix of a slab structure with three media and refractive indexes $n_1$, $n_2$, $n_3$ is

$$S_{11} = \frac{\Gamma_{12} + \Gamma 23 e^{-j2\Psi}}{1 + \Gamma_{12}\Gamma_{23}^{-j2\Psi}} \quad (4)$$

where $\Gamma_{12}$ and $\Gamma_{23}$ are the reflection coefficient at the interface between media 1-2 and media 2-3 and $\Psi$ is the propagation factor. By propagating the reflection effect from the outmost to the innermost layer the $S_{11Tot}$ of the full structure can be derived.

While attenuation losses are for sure to be considered but limited, the most impacting factor in such a structure is the $S_{11Tot}$ which needs to be as small as possible to avoid ghost target appearances and Signal to Noise Ratio (SNR) degradation. From the $tan\delta$ measurements and layer thicknesses the one-way attenuation losses of the structure at 77 GHz have been estimated to be 0.6 dB which is a comparable value with respect to the ones of typical bumpers [22]. Since changing the petal materials was not possible, the thickness of the petal outer layers was optimized with the goal of mitigating the reflection coefficient in the full 77-81 GHz frequency band. The optimal thickness for the petal outer screen is 2.2 mm.

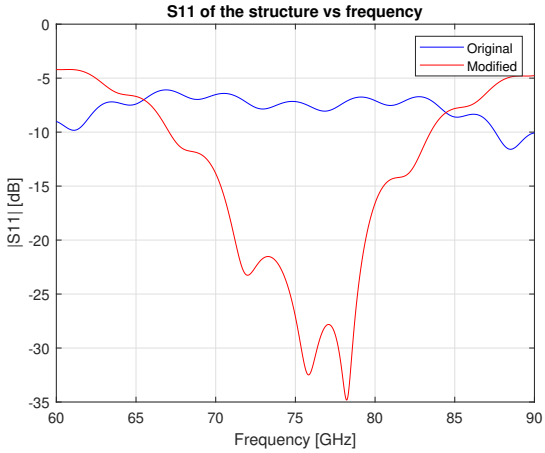



Fig. 3: Reflection coefficient of the lamp structure in front of the radar vs frequency with original and optimized thickness of the petal outer screen

Fig. 3 shows the $S_{11Tot}$ of the multi-layer structure in front of the radar for the 60-90 GHz frequency band with two different thicknesses of the petal outer screen material (original and optimized). Drastic improvements of $S_{11Tot}$ have been obtained. In the original case the $S_{11Tot}$ was worst than -7 dB from 77-81 GHz while with the optimized thickness the reflection coefficient is below -18 dB in the 77-79.5 GHz frequency band and as good as -12 dB up to 81 GHz.

## IV. Hardware Design

For the system design, since the petal has limited dimensions of 60 mm x 29 mm, a two boards solution has been considered: the radar power supply board, which generates the necessary low noise power rails and manages the communication of the radar with the outside world, and the radar board which hosts the integrated radar chip, the transmitting and receiving antennas, the voltage supply filters, and the other required components to handle communication.

The radar board dimensions are 57 mm x 27 mm x 1.6 mm and it fits into the petal slot. The radar power supply board, needs to fit into the lamp orthogonally connected to the radar board. Mechanical constraints have constrained components placing in some areas of the radar power supply board and led to the final form and dimensions of Fig. 4. The radar power supply board fits into the lamp housing and it has been stabilized with mechanical holders to minimize vibrations.

Authorized licensed use limited to: Politecnico di Torino. Downloaded on October 22,2023 at 08:47:04 UTC from IEEE Xplore. Restrictions apply.
© 2023 IEEE. Personal use is permitted, but republication/redistribution requires IEEE permission. See https://www.ieee.org/publications/rights/index.html for more information.

This article has been accepted for publication in IEEE Transactions on Vehicular Technology. This is the author's version which has not been fully edited and content may change prior to final publication. Citation information: DOI 10.1109/TVT.2023.3324986



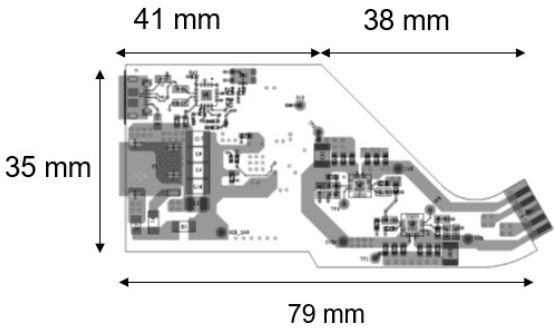



Fig. 4: Radar power supply board final form (Top Layer)

The radar selected chip is the AWR1843 [27] manufactured by Texas Instruments. It is an integrated single chip radar sensor based on the 45 nm Radio Frequency Complementary Metal-Oxide Semiconductor (RFCMOS) and operates in the entire 76–81 GHz automotive frequency band. To generate FMCW signal at the desired carrier frequency, an internal 40 MHz crystal oscillator followed by a clean-up Phased Locked Loop (PLL) and a Radio Frequency (RF) synthesizer circuit are used. From the 20 GHz synthesized signal a 4X multiplier generates the proper signals for the Transmitters (TXs) and the Receivers (RXs).

An RF noise figure of 15 dB and a phase noise at 1 MHz offset in the 77-81 GHz band of -93 dBc/Hz are specified by the producer. Operations with 3 TXs and 4 RXs with In-phase and Quadrature (IQ) channels are fully supported. The chip integrates an R4F ARM processor for automotive interfacing and a high performance C674x Digital Signal Processor (DSP) for the radar signal processing.

The radar power supply board and the radar board are connected to each other and they work as an integrated solution as shown in the block diagram of Fig. 5. The radar outputs are transmitted via Serial Peripheral Interface (SPI) through the radar power supply board to a KSZ8851SNL [28] evaluation board (SPI-to-Ethernet converter) and then to a laptop PC to be displayed on a user interface and to be stored for further post-processing. Commands are transmitted from the laptop PC through Ethernet to the KSZ8851SNL and then, via SPI to the radar.

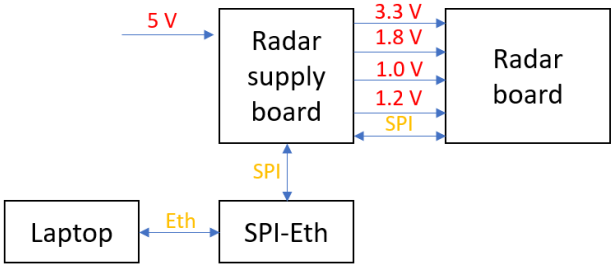



Fig. 5: Radar prototype block scheme

Fig. 6 and Fig. 7 report a block diagram, for both the radar power supply board and the radar board. The input power required by the AWR1843 chip are generated from a 5V power supply. A MAX1502 [29] DC-DC dual buck switching regulator generates the 3.3 V voltage, used by the SPI communication interfaces, and the 1.8 V voltage, used by the RF VCO, internal clock module and base-band circuitry. The switching frequency is set to 2 MHz. Due to the very high sensitivity of the radar sensor toward noise on the supply voltage, it has been necessary to strongly filter the harmonics generated by the DC-DC converter. The 1.24 V rail is required to supply the embedded ARM processor and DSP while 1.0 V is required to supply the RF chain. Both voltages are obtained with TPS7A5301 [30] low noise, low drop out regulators.

All the components installed on the the radar power supply board are automotive compliant (AEC-Qxx qualified [31]) and can be integrated on the original lamp mother board, with full integration of the solution.

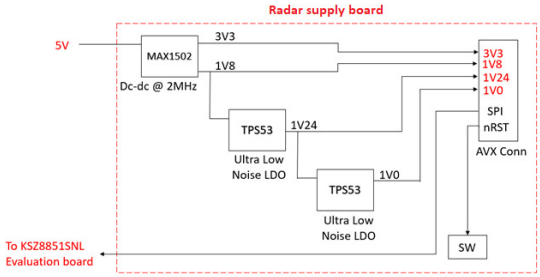



Fig. 6: Radar power supply board block diagram

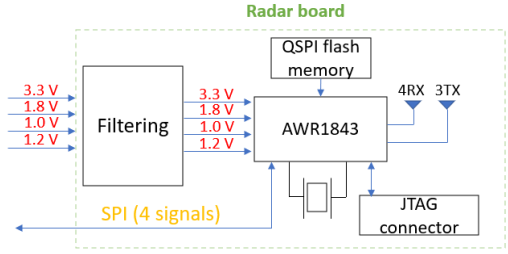



Fig. 7: Radar board block diagram

The radar board hosts the AWR1843 chip, a 40 MHz crystal oscillator, a QSPI memory for booting [32], filters, the JTAG connector for debug purpose, the connector for power supply and SPI communication and the antennas. Since the AWR1843 is not transmitting continuously, it requires high impulsive currents. The connector between the two boards has been chosen with high current rating per pin (2.5 A) and it has been selected as the 00-9159-650 [27] from AVX. The connector is installed in such a way that the power board can be inserted orthogonally into the radar board. With minimal change in the radar board connector the radar board can be directly plugged into the original lamp mother board-integrated with the radar power supply board components, supplied from the 12 V car battery and communicating on the car CAN bus as shown in Fig 8.

Both the transmitting and receiving antennas are vertically polarized microstrip patch arrays of 4 elements printed on a

Authorized licensed use limited to: Politecnico di Torino. Downloaded on October 22,2023 at 08:47:04 UTC from IEEE Xplore. Restrictions apply.
© 2023 IEEE. Personal use is permitted, but republication/redistribution requires IEEE permission. See https://www.ieee.org/publications/rights/index.html for more information.

This article has been accepted for publication in IEEE Transactions on Vehicular Technology. This is the author's version which has not been fully edited and content may change prior to final publication. Citation information: DOI 10.1109/TVT.2023.3324986



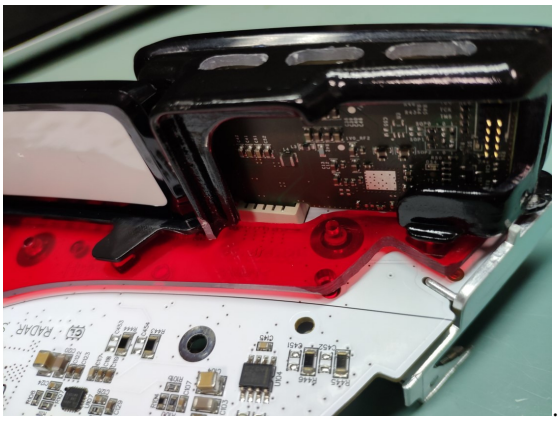


Fig. 8: Radar board slotted into the petal and plugged into the original lamp mother board integrated with power supply board components

ROGER4835 [33] substrate ($\epsilon_r$=3.48) with a 10 dB gain at 77 GHz, $\pm 28°$ horizontal 3dB-beamwidth and $\pm 14°$ vertical 3dB-beamwidth. All the antennas are positioned behind the petal and with a clear field of view not limited by the lamp structure. The antenna are disposed on the radar board to obtain a uniform MIMO virtual array with one 8 element row ad a second 4 element row displaced in elevation as in the scheme of Fig. 9. This configuration enables both azimuth and

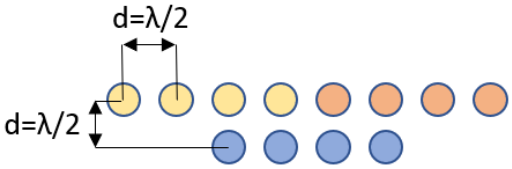



Fig. 9: MIMO virtual array

elevation direction of arrival estimation. The virtual elements are spaced of a distance $d = \frac{\lambda}{2}$ horizontally and vertically in order to maximize the field of view.

Fig. 10 shows the solution outside the lamp with the two manufactured boards connected together and the SPI to Ethernet conversion board dedicated to communicate data to a laptop user interface.

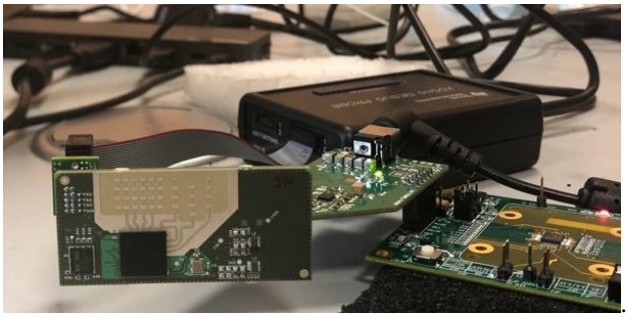


Fig. 10: Realized Radar board prototype

## V. Software Design

The beat frequency I and Q signals sampled with the internal ADCs are processed by the AWR1843's DSP according to the diagram of Fig. 11. Range and Doppler FFTs are performed on the captured data, a detection layer is then applied to the obtained Doppler-Range matrix by means of Constant False Alarm Rate (CFAR) algorithms [34] in both directions. All the cells of the two dimension FFT matrix which pass the CFAR thresholding form the so called point cloud on which direction of arrival estimation is performed. The obtained point cloud is sent to the AWR1843 R4F ARM processor as input for the tracking layer to predict the future states and compute confidence level of the trace and estimate dimensions of the targets. The processor outputs via SPI the list of targets with different attributes and separated to distinguish between moving and static ones.

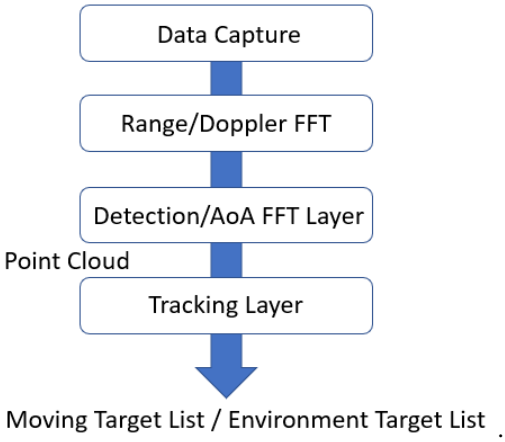



Fig. 11: Radar processing overview

The attributes provide targets position, velocity, dimensions and SNR of the detected peaks.

A two frame structure is used for the transmitted signal configuration as shown in Fig. 12. In the first frame the three TXs use the Time Division Multiplexing (TDM) MIMO scheme for azimuth and elevation direction of arrival. All the TXs in this frame use linear frequency modulated signal with the same duration and slope and whose parameters are reported in Table II.

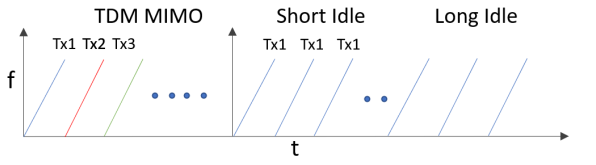



Fig. 12: Frame structure

The second frame has two burst of linear frequency modulated signal which are sent with only one TX and whose parameter are reported in Table III. They have different idle time in order to have different Pulse Repetition Frequency (PRF) and consequently different maximum unambiguous

Authorized licensed use limited to: Politecnico di Torino. Downloaded on October 22,2023 at 08:47:04 UTC from IEEE Xplore. Restrictions apply.
© 2023 IEEE. Personal use is permitted, but republication/redistribution requires IEEE permission. See https://www.ieee.org/publications/rights/index.html for more information.

This article has been accepted for publication in IEEE Transactions on Vehicular Technology. This is the author's version which has not been fully edited and content may change prior to final publication. Citation information: DOI 10.1109/TVT.2023.3324986



TABLE II: Key Radar Parameters for the TDM MIMO frame

| Symbol | Description | Value |
|---|---|---|
| BW | Bandwidth | 457 MHz |
| Tc | Chirp Duration | 50.57 $\mu s$ |
| S | Slope | 12.5 MHz/s |
| N | Number of chirps per TX | 64 |
| $Fs$ | sampling frequency | 7 MHz |

TABLE III: Key Radar Parameters for the second frame

| Symbol | Description | Value |
|---|---|---|
| BW | Bandwidth | 457 MHz |
| Tc1 | Chirp Duration | 50.57 $\mu s$ |
| Tc2 | Chirp Duration | 55.57 $\mu s$ |
| S | Slope | 12.5 MHz/s |
| N | Number of chirps per TX | 64 |
| $Fs$ | sampling frequency | 7 MHz |

velocities. In this way it is possible to estimate velocity larger than the maximum unambiguous one.

In the following we describe the most peculiar software module of the system.

*1) Unambiguous Doppler Estimation:* If we consider a target with radial velocity $v_t$ its Doppler frequency shift $f_d$ is:

$$f_d = \frac{2v_t}{\lambda}. \tag{5}$$

If the Doppler frequency shift is larger than half of the PRF, the velocity is ambiguous and the Doppler shift satisfy the equation:

$$f_d = f_{meas} \pm nPRF. \tag{6}$$

Our approach to recover the original velocity is the application of the Chinese reminder theorem as shown in [35] and [36]. It requires the adoption of two PRFs as in the second frame of our transmitted signals. The PRFs need to be pairwisely coprime and a system of congruence need to be solved to find the correct integer value n and therefore $f_d$.

To implement our solution we apply a cycle of tries (NTRY) for the different values of n for each PRFs and we look for the minimum error between the frequency shift of the different PRFs.

The pseudo-code of the algorithm is here reported.

**Algorithm 1** Pseudo-code of the algorithm for Doppler disambiguation.

```
for i = 0; i < NTRY; i++
{fd1 = fmeas1 + (i − (NTRY − 1)/2) ∗ PRF1;
    for j = 0; j < NTRY; j++
    {fd2 = fmeas2 + (j − (NTRY − 1)/2) ∗ PRF2;
        if (abs(fd1 − fd2) < minToll)
        {minToll = abs(fd1 − fd2);
         fdreal = fd1;
        }
    }
}
```

An example of the algorithm result for $NTRY = 3$ is reported in the graph of Fig. 13: the blue curve is the range of real velocities of the target; the red and yellow curves represent the velocities measured with the two PRFs limited by the ambiguity, and the purple curve shows the recovered velocities which, in this cases match the real one. With $NTRY = 3$, the unambiguous velocity is extended up to 3 times (both in the positive and negative direction) with respect to the original ones. Increasing the number of tries can extend further the velocity range.

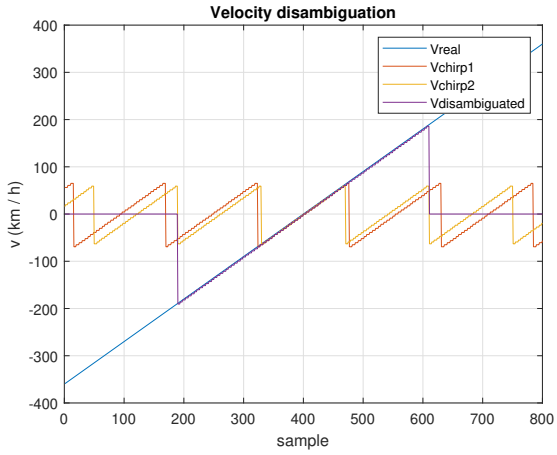



Fig. 13: Velocity disambiguated with two PRFs and NTRY=3

*2) Doppler induced phase error compensation:* The TDM-MIMO frame allows to obtain a better direction of arrival resolution but, in non-stationary scenario, the phase error induced by the switching time $T_r$ between different TXs must be compensated.

In general for M TXs the error due to the m-th TX at the same RX is [37]

$$\Delta\tilde{\phi}_{Tx_m} = 2\pi f_d T_r \frac{m-1}{M}. \tag{7}$$

Thanks to the estimated target Doppler frequency, a correction of the input signals for the direction of arrival calculation in the TDM-MIMO frame is performed.

*3) Tracking:* The targets detected by the radar are grouped by means of a scoring function and elliptical gating [38].

The tracking is performed on the centroids of the obtained point cloud with a multidimensional Kalman filter [39] with 3 inputs (range, angle, radial velocity) and 4 states (x, y, $V_x$, $V_y$).

*4) Ghost Target Removal:* The effect of multipath propagation gives rise to the possible appearance of ghost targets. In our application a similar approach to the one proposed in [40] is adopted to tackle this problem.

From the estimated values of range at which ghost targets typically appear, a threshold ($\Delta R_{th}$) on the difference of distance between the ghost target and the real one can be obtained. If a tracked target is within $\Delta R_{th}$ from another, then it is marked as a probable ghost. To confirm the ghost presence, a velocity check is performed. The ghost velocity measure is usually similar to the one of the real target even if it can differ slightly since the multipath has a different direction

Authorized licensed use limited to: Politecnico di Torino. Downloaded on October 22,2023 at 08:47:04 UTC from IEEE Xplore. Restrictions apply.
© 2023 IEEE. Personal use is permitted, but republication/redistribution requires IEEE permission. See https://www.ieee.org/publications/rights/index.html for more information.

This article has been accepted for publication in IEEE Transactions on Vehicular Technology. This is the author's version which has not been fully edited and content may change prior to final publication. Citation information: DOI 10.1109/TVT.2023.3324986



of arrival. Therefore, if the difference of velocities of the real target and the ghost candidate is within a certain limit, the ghost is confirmed and removed from the target list.

## VI. Thermal Measurements

For automotive standards, chip temperature must be controlled carefully, up to 70 °C ambient temperature. Heat chamber measurements of the radar system have been performed to verify that maximum value of the radar chip junction temperature (the internal semiconductors temperature) stays below $T_{jmax} = 125$ °C.

In Fig. 14 a heat map of the running radar at ambient temperature outside the lamp is reported showing low values for the measured temperature.

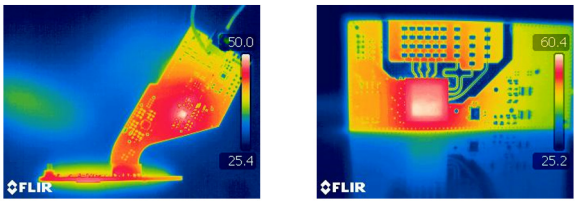



Fig. 14: Thermal camera photos of the boards at 25 °C

The radar inserted in the lamp has been tested with lighting and electronics turned on, at different temperatures, in the heat chamber. A thermoucouple sensor was attached to the case of the radar chip to measure the case temperature $T_c$ and derive the internal junction temperature $T_j$ as

$$T_j = T_c + \theta_{JC} P_d \tag{8}$$

where $\theta_{JC}$ is the case to junction thermal resistance specified on the data sheet and $P_d$ is the average power consumption of the chip. The average power consumption of the running radar has been measured, on each power supply rail, by measuring the absorbed current with an oscilloscope and the results are reported in TABLE IV.

| Voltage rail | Mean current [mA] | Power consumption[W] |
|---|---|---|
| 1.0V | 70 | 0.056 |
| 1.24V | 556 | red 690 |
| 1.8V | 155 | 236 |
| 3.3V | 24 | 0.082 |
| Total on RF board | | 1.15 |

TABLE IV: Power consumption of the RF board

The radar and lamp set-up in the heat chamber is shown in Fig. 15.

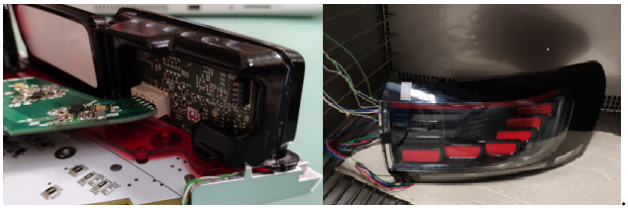


Fig. 15: Measurement Set-Up

The heat chamber was set at 40 °C, 60 °C, and 70 °C. When the temperature was reached, radar and light were turned on and the thermocouple values were read after 30 minutes of operations. The measured case temperatures $T_c$ and the derived $T_j$, assuming the power consumption of TABLE IV, are reported in TABLE V. Only in the worst case scenario, with heat chamber temperature at 70 °C the $T_j = 129°C$ exceeds the maximum rating ($T_{jmax} = 125$°C).

Some improvements in the structure of the lamp for air convection and in component placing on the radar board will be required to solve this issue.

| $T_{test}$[°C] | $T_{case}$ [°C] | $T_j$ [ °C] |
|---|---|---|
| 40 | 101 | 106 |
| 60 | 106 | 111 |
| 70 | 124 | 129 |

TABLE V: Thermal tests of radar in the lamp at different working temperatures

## VII. Test Results

The radar has been tested at first in an open field to verify functionality of the system when a 10 dBsm corner reflector has been positioned 16 meters at boresight with the radar outside the lamp, inside the lamp with the original petal and inside the lamp with the optimized petal. In Fig. 16 the range responses in the three scenarios, non-coherently integrated over multiple frames (3 minutes time windows) and averaged over time are shown and the peak amplitudes generated by the corner reflector are marked by the black lines. When the radar is inside the lamp with the original petal, the peak amplitude is 4.5 dB lower with respect to case when the radar is outside the lamp. With the optimized petal thickness, the peak amplitude is 1.2 dB lower confirming the simulation results of Fig. 3 (negligible attenuation due to reflections) and showing a significant improvement.

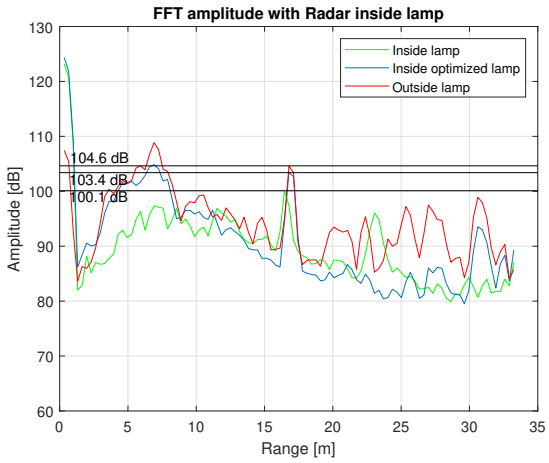



Fig. 16: 10 dBsm corner reflector non-coherently averaged peak amplitude inside and outside lamp with different petal material thickness

Another set of experiments have been performed to test the radar performances versus range. A 10 dBsm corner reflector

Authorized licensed use limited to: Politecnico di Torino. Downloaded on October 22,2023 at 08:47:04 UTC from IEEE Xplore. Restrictions apply.
© 2023 IEEE. Personal use is permitted, but republication/redistribution requires IEEE permission. See https://www.ieee.org/publications/rights/index.html for more information.

This article has been accepted for publication in IEEE Transactions on Vehicular Technology. This is the author's version which has not been fully edited and content may change prior to final publication. Citation information: DOI 10.1109/TVT.2023.3324986



has been moved from 0 to 75 meter on the boresight. The range response amplitudes of the moving target at its Doppler index (blue curve), as well as the averaged noise floor at the Doppler index of the target of the moving target (red curve) and the maximum value of the noise floor at the Doppler index of the moving target (green curve) are reported in Fig. 17. The radar response shows continuous detection over all ranges and a SNR of 11.5 dB at the maximum range of 75 m still good for reliable detection.

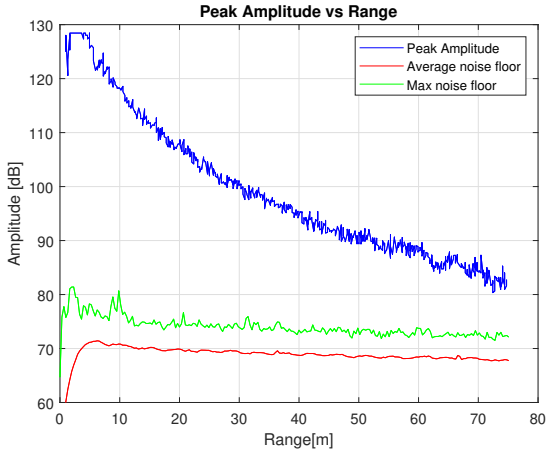



Fig. 17: FFT peaks of the corner reflector vs range 75 m

The radar vehicles detection and tracking has been extensively tested in the backyard of our institute. A series of tests has been performed in an open field with a 10 dBsm corner reflector moved on a "S" shape path. The radar detects the target each frame with multiple points: the point cloud points (blue and green dot) enable the tracking algorithm to follow the targets even when the movement is transversal to the radar radial direction as shown in Fig. 18.

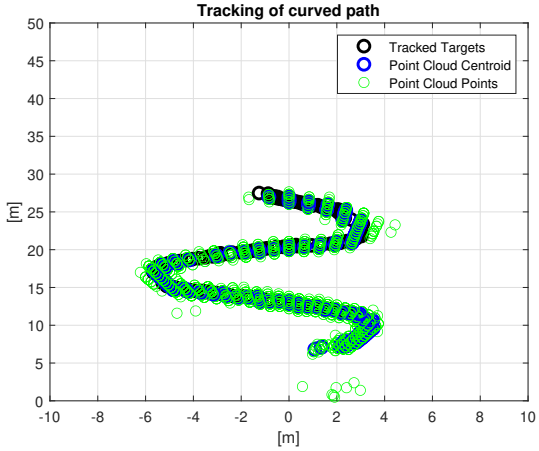



Fig. 18: Tracking of a "S" shape path with corner reflector

Relevant tests have been performed on the road with realistic traffic scenarios. Several data on different days, times, and traffic conditions have been collected to test algorithms and radar performances. A typical scenario is reported in Fig. 19 where we look at a four lanes (two per traffic direction) road. The lamp equipped with the radar has been positioned on a static support between the two traffic directions slightly closer to one of the two and pointing upwards.




Fig. 19: Top view of a road used for the radar tests

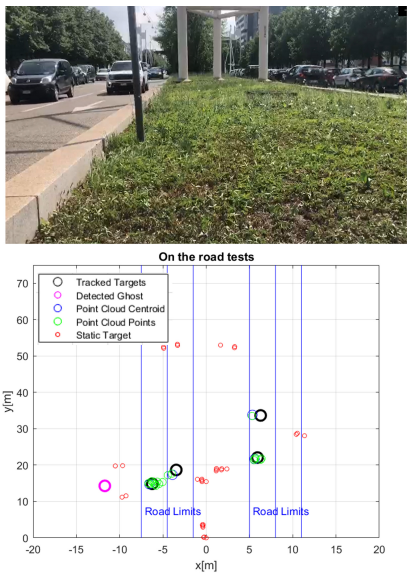



Fig. 20: Radar test on the road

Fig. 20 shows a snap of the video collected during the test and the real time processed radar output. In the reported example, two cars are approaching the radar at similar speeds near to each other and two cars are moving in the other direction in the same lane.

All the moving cars are tracked (black dots) correctly in their respective lanes; a moving ghost target due to multipath reflections is identified and removed by the ghost removal algorithm (pink dots). The poles, trees and some of the parked cars are detected as static targets (red dots). The blue lines limiting the road have been added in post processing. During the tests, out of 437 vehicles followed by the tracking algorithm, 96.2% of them have been successfully tracked inside the correct lane. The wrong predictions have been due to heavy traffic occluding targets or to not enough resolution to separate very close targets at similar angle, speed and range.

A final set of tests has been performed to verify the detection of crossing bicycle and pedestrian. The radar has been positioned at 30° angle with respect to a bicycle lane. In Fig. 21 a bicycle has been successfully tracked while

Authorized licensed use limited to: Politecnico di Torino. Downloaded on October 22,2023 at 08:47:04 UTC from IEEE Xplore. Restrictions apply.
© 2023 IEEE. Personal use is permitted, but republication/redistribution requires IEEE permission. See https://www.ieee.org/publications/rights/index.html for more information.

This article has been accepted for publication in IEEE Transactions on Vehicular Technology. This is the author's version which has not been fully edited and content may change prior to final publication. Citation information: DOI 10.1109/TVT.2023.3324986



crossing from left to right. Two pedestrian crossing in the other direction have been detected but not tracked due to their low velocity. The poles near the lane and the wall are detected correctly as static targets.

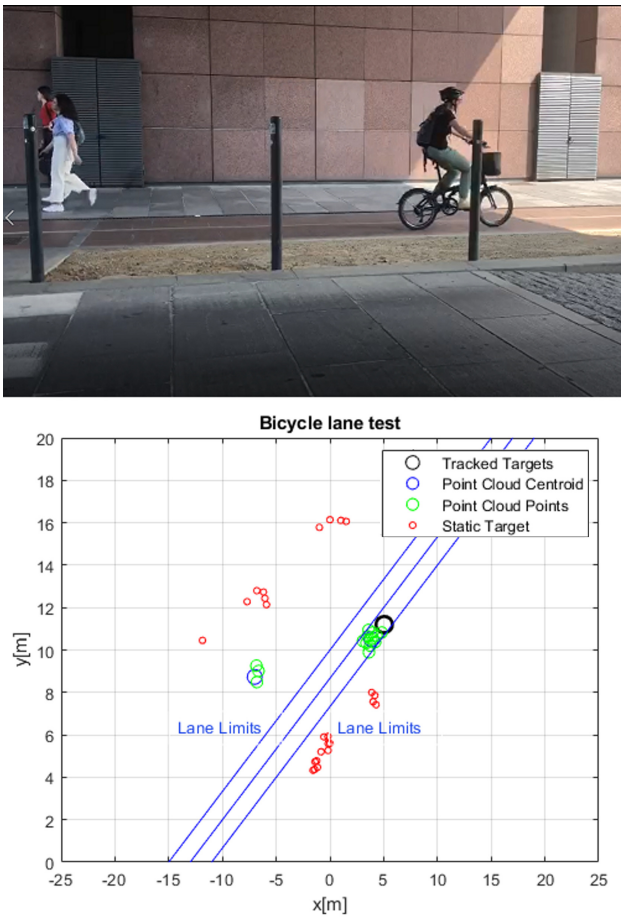



Fig. 21: Bicycle lane test

## VIII. Conclusion

Radar sensors are commonly installed as blackboxes behind bumpers. We have shown that the full integration of an automotive FMCW-MIMO 77-81 GHz radar sensor into a rear lamp is possible following the described approach. This solution can bring various advantages regarding performances, protections, and installation convenience. The radar installed into the lamp has been successfully prototyped and tested. The materials of the lamp have been optimized to reduce reflections and to improve SNR of the received signals.

Preliminary temperature tests required by automotive standards have been performed with the radar operating inside the lamp. The results suggest that the heat distribution of the board should be slightly improved.

To evaluate the performances, tests have been carried out in an open field and on the road and optimal results for the detection and tracking of vehicles and bicycles have been obtained up to 75 m range.

## References

[1] V. K. Kukkala, J. Tunnell, S. Pasricha, and T. Bradley, "Advanced driver-assistance systems: A path toward autonomous vehicles," IEEE Consumer Electronics Magazine, vol. 7, no. 5, pp. 18–25, 2018.

[2] "Society of automotive engineering site," (Accessed on 06/08/2023). [Online]. Available: http://www.SAE.org

[3] C. Waldschmidt, J. Hasch, and W. Menzel, "Automotive radar — from first efforts to future systems," IEEE Journal of Microwaves, vol. 1, no. 1, pp. 135–148, 2021.

[4] S. Roehr, P. Gulden, and M. Vossiek, "Precise distance and velocity measurement for real time locating in multipath environments using a frequency-modulated continuous-wave secondary radar approach," IEEE Transactions on Microwave Theory and Techniques, vol. 56, no. 10, pp. 2329–2339, 2008.

[5] C. Sturm and W. Wiesbeck, "Waveform design and signal processing aspects for fusion of wireless communications and radar sensing," Proceedings of the IEEE, vol. 99, no. 7, pp. 1236–1259, 2011.

[6] A. Bourdoux, U. Ahmad, D. Guermandi, S. Brebels, A. Dewilde, and W. V. Thillo, "Pmcw waveform and mimo technique for a 79 ghz cmos automotive radar," 2016 IEEE Radar Conference (RadarConf), pp. 1–5, 2016.

[7] K. V. Mishra, M. Bhavani Shankar, V. Koivunen, B. Ottersten, and S. A. Vorobyov, "Toward millimeter-wave joint radar communications: A signal processing perspective," IEEE Signal Processing Magazine, vol. 36, no. 5, pp. 100–114, 2019.

[8] J. A. Zhang, F. Liu, C. Masouros, R. W. Heath, Z. Feng, L. Zheng, and A. Petropulu, "An overview of signal processing techniques for joint communication and radar sensing," IEEE Journal of Selected Topics in Signal Processing, vol. 15, no. 6, pp. 1295–1315, 2021.

[9] G. K. Carvajal, M. F. Keskin, C. Aydogdu, O. Eriksson, H. Herbertsson, H. Hellsten, E. Nilsson, M. Rydström, K. Vänas, and H. Wymeersch, "Comparison of automotive fmcw and ofdm radar under interference," in 2020 IEEE Radar Conference (RadarConf20), 2020, pp. 1–6.

[10] M. Caffa, F. Biletta, and R. Maggiora, "Binary-phase vs. frequency modulated radar measured performances for automotive applications," Sensors, vol. 23, no. 11, 2023. [Online]. Available: https://www.mdpi.com/1424-8220/23/11/5271

[11] M. Bauduin and A. Bourdoux, "Code diversity for range sidelobe attenuation in pmcw and ofdm radars," in 2021 IEEE Radar Conference (RadarConf21), 2021, pp. 1–5.

[12] J. Hasch, E. Topak, R. Schnabel, T. Zwick, R. Weigel, and C. Waldschmidt, "Millimeter-wave technology for automotive radar sensors in the 77 ghz frequency band," IEEE Transactions on Microwave Theory and Techniques, vol. 60, no. 3, pp. 845–860, 2012.

[13] D. Bliss and K. Forsythe, "Multiple-input multiple-output (MIMO) radar and imaging: degrees of freedom and resolution," in The Thrity-Seventh Asilomar Conference on Signals, Systems Computers, 2003, vol. 1, 2003, pp. 54–59 Vol.1.

[14] C. Pfeffer, R. Feger, C. Wagner, and A. Stelzer, "Fmcw mimo radar system for frequency-division multiple tx-beamforming," IEEE Transactions on Microwave Theory and Techniques, vol. 61, no. 12, pp. 4262–4274, 2013.

[15] S. Sun, A. P. Petropulu, and H. V. Poor, "Mimo radar for advanced driver-assistance systems and autonomous driving: Advantages and challenges," IEEE Signal Processing Magazine, vol. 37, no. 4, pp. 98–117, 2020.

[16] "Arbe robotics radar page," (Accessed on 08/08/2023). [Online]. Available: https://arberobotics.com/perception-radar

[17] "Uhnder s80 chip pmcw automotive band radar," (Accessed on 08/08/2023). [Online]. Available: https://www.uhnder.com/images/data/S80_PTB_Rev1.0_May_5_2022_.pdf

[18] "Vayyar 79 ghz radar page," (Accessed on 08/08/2023). [Online]. Available: https://vayyar.com/auto/technology/79ghz/

[19] M. Gottinger, M. Hoffmann, M. Christmann, M. Schütz, F. Kirsch, P. Gulden, and M. Vossiek, "Coherent automotive radar networks: The next generation of radar-based imaging and mapping," IEEE Journal of Microwaves, vol. 1, no. 1, pp. 149–163, 2021.

[20] A. Correas-Serrano, M. Gonzalez-Huici, R. Simoni, T. Bredderman, E. Warsitz, T. Müller, and O. Kirsch, "Performance analysis and design of a distributed radar network for automotive application," in 2022 23rd International Radar Symposium (IRS), 2022, pp. 30–35.

[21] R. Schnabel, D. Mittelstrab, T. Binzer, C. Waldschmidt, and R. Weigel, "Reflection, refraction, and self-jamming," IEEE Microwave Magazine, vol. 13, no. 3, pp. 107–117, 2012.

Authorized licensed use limited to: Politecnico di Torino. Downloaded on October 22,2023 at 08:47:04 UTC from IEEE Xplore. Restrictions apply.
© 2023 IEEE. Personal use is permitted, but republication/redistribution requires IEEE permission. See https://www.ieee.org/publications/rights/index.html for more information.

This article has been accepted for publication in IEEE Transactions on Vehicular Technology. This is the author's version which has not been fully edited and content may change prior to final publication. Citation information: DOI 10.1109/TVT.2023.3324986



[22] J. C. Dash, M. Parikh, N. Modi, J. Mukherjee, S. VR, T. SaiDeepak, and V. Dhoot, "Performance evaluation of automotive radar in the presence of bumper with multiple paint layers using bidirectional loss model," in 2021 15th European Conference on Antennas and Propagation (EuCAP), 2021, pp. 1–5.
[23] F. Norouzian, E. Marchetti, E. G. Hoare, M. Gashinova, C. C. Constantinou, P. Gardner, and M. Cherniakov, "Experimental study on low-thz automotive radar signal attenuation during snowfall," IET Radar, Sonar & Navigation, 2019.
[24] S. Hamid, D. Heberling, M. Junghähnel, T. Preussner, P. Gretzki, L. Pongratz, C. Hördemann, and A. Gillner, "Optically transparent antenna integrated inside a headlamp for automotive radar application," in 2020 14th European Conference on Antennas and Propagation (EuCAP), 2020, pp. 1–5.
[25] N. Y. K. K. W. Yamamura, "Millimeter wave radar-equipped headlamp," 2014, uS Patent: US8803728B2.
[26] G. Hakobyan and B. Yang, "High-performance automotive radar: A review of signal processing algorithms and modulation schemes," IEEE Signal Processing Magazine, vol. 36, no. 5, pp. 32–44, 2019.
[27] "Texas instrument site, awr1843 product page." [Online]. Available: https://www.ti.com/product/AWR1843(Accessedon1/09/2021
[28] "Microchip site , ksz8851snl-eval product page." [Online]. Available: https://www.microchip.com/en-us/development-tool/KSZ8851SNL-EVAL(Accessedon20/12/2021)
[29] "Maxim integrated." [Online]. Available: https://www.maximintegrated.com/en/products/power/switching-regulators/MAX15062.html(Accessedon09/01/2022)
[30] "Texas instruments site, tps7a53-q1 product page." [Online]. Available: https://www.ti.com/product/TPS7A53-Q1
[31] "Aec council site," (Accessed on 10/02/2022). [Online]. Available: http://www.aecouncil.com
[32] "Macronix site , mx25v1635l product page." [Online]. Available: https://www.mxic.com.tw/en-us/products/NOR-Flash/Serial-NOR-Flash/Pages/spec.aspx?p=MX25V1635F&m=Serial+NOR+Flash&n=PM2257(Accessedon23/12/2021)
[33] "ROGERS Corporation Site, RO4835 Laminates Page." [Online]. Available: https://rogerscorp.com/advanced-electronics-solutions/ro4000-series-laminates/ro4835-laminates(Accessedon25/09/2021)
[34] Principles of modern radar / ed. by Jerry L. Eaves and Edward K. Reedy. New York: Van Nostrand Reinhold, 1987.
[35] F. D. A. García, A. S. Guerreiro, G. R. d. L. Tejerina, J. C. S. S. Filho, G. Fraidenraich, and M. D. Yacoub, "Doppler estimation for high-velocity targets using subpulse processing and the classic chinese remainder theorem," 2021. [Online]. Available: https://arxiv.org/abs/2101.11311(Accessedon12/10/2021)
[36] B. Silva and G. Fraidenraich, "Performance analysis of the classic and robust chinese remainder theorems in pulsed doppler radars," IEEE Transactions on Signal Processing, vol. 66, no. 18, pp. 4898–4903, 2018.
[37] J. Bechter, F. Roos, and C. Waldschmidt, "Compensation of motion-induced phase errors in TDM MIMO radars," IEEE Microwave and Wireless Components Letters, vol. 27, no. 12, pp. 1164–1166, 2017.
[38] S. S. Blackman, Design and analysis of modern tracking systems, ser. Artech House radar library. Boston, Mass. ; London: Artech House, 1999.
[39] E. Brookner, Tracking and Kalman filtering made easy. New York: Wiley, 1998.
[40] C. Liu, S. Liu, C. Zhang, Y. Huang, and H. Wang, "Multipath propagation analysis and ghost target removal for FMCW automotive radars," in IET International Radar Conference (IET IRC 2020), vol. 2020, 2020, pp. 330–334.



**Mattia Caffa** graduated in electronic engineering at the Politecnico di Torino, Turin, Italy, in 2020. He received the M.Sc. degree in electrical and computer engineering from the University of Illinois, Chicago, IL, USA, in 2020. He is currently pursuing a Ph.D. degree in electronic engineering at Politecnico di Torino. His main research interests includes embedded signal processing, automotive radars design, firmware development and testing.



**Stefano Bottigliero** received the M.Sc. degree in electronic engineering from the Politecnico of Torino, Turin, Italy, in 2017 and the Ph.D degree in electronic engineering from the Politecnico of Torino in 2022. His main research interests include localization systems, printed circuit board (PCB) design for high-frequency applications, and automotive radars.



**Federico Ramonda** received the M.Sc. degree in electronic engineering from the Politecnico of Torino, Turin, Italy, in 2016. He is an innovation and advanced engineering electronic designer at Magna Lighting Europe in Turin since 2018.



**Luca Gioanola** Luca Gioanola, received the Ph.D. degree in electronic and communication engineering from the Politecnico of Torino, Turin, Italy, in 2008. He is the Innovation and Advanced Engineering Manager in Magna Lighting Europe, Turin.



**Riccardo Maggiora** is currently an Engineer and a Professor with the Politecnico di Torino, Turin,Italy. He has been directing, for more than a decade, the Laboratory on Radar Systems and Antennas, Politecnico di Torino. He is responsible for the development and implementation of various radar and localization systems for the aerospace, automotive, and industrial sector. He is the author of numerous scientific articles.

Authorized licensed use limited to: Politecnico di Torino. Downloaded on October 22,2023 at 08:47:04 UTC from IEEE Xplore. Restrictions apply.
© 2023 IEEE. Personal use is permitted, but republication/redistribution requires IEEE permission. See https://www.ieee.org/publications/rights/index.html for more information.